The investigation of the topographical effect on multi-scale Eastward-Moving Southwest Vortex from the perspective of PV theory

Chao Li[1,2], Yan Li[1], Shenming Fu[3], Xingwen Jiang[4], Xiaofang Wang[2], Shanshan Li[2], Chunguang Cui[2],Yang Hu[2], Wenjun Cui[5]

1. College of Atmospheric Sciences, Lanzhou University, Lanzhou, China
2. Hubei Key Laboratory for Heavy Rain Monitoring and Warning Research, Institute of Heavy Rain, China Meteorological Administration, Wuhan, China
3. Institute of Atmospheric Physics, Chinese Academy of Sciences, Beijing, China
4. Institute of Plateau Meteorology, China Meteorological Administration, Chengdu, China
5. Cooperative Institute for Mesoscale Meteorological Studies, Oklahoma University, Norman, United States

Abstract: Multi-scale Eastward-Moving Southwest Vortex (EMSV) inducing severe rainstorms frequently occurs in the middle and lower reaches of Yangtze River Basin (YRB). The Second-Step Terrain Region (SSTR) located in the middle reaches of YRB have significant role in strengthening this synoptic system. This paper systematically studies the topographical effect of SSTR based on the WRF synthetic simulation of three multi-scale EMSV cases that occurred in 2015 and 2016. Results show that the compound circulation simulated by WRF can be decomposed into the meso-scale balanced circulation and the local-scale perturbed circulation with the application of the Piecewise Potential Vortex Inversion (PPVI) technique. The cyclonic perturbed circulation has a closer relationship with the occurrence of local heavy precipitation compared to the balanced circulation. Moreover, the good agreement between the positive Potential Vortex (PV) anomalies and the cyclonic perturbed circulation suggests that the persistence of the cyclonic perturbed circulation highly depends on the positive PV anomalies. Besides, the qualitative sensitivity experiments reveal that the topographical effect stimulates the genesis of the positive PV anomalies mainly by strengthening the latent heat release associated with the updraft, and the latent heat release associated with the cyclonic eddy. The quantitative diagnosis of the source of the PV anomalies shows that the former one contributes more to the genesis of the positive PV anomalies than the latter one. Further quantitative diagnosis of the updraft reveals that the topographical lifting effect is identified as the main mechanism in strengthening the updraft within the topography region.

1. Introduction

The mesoscale convective activities are highly active within the latitudinal zone

of 30° N, where most of Yangtze River Basin (YRB) is located (Zheng, et al., 2008; Yang, et al., 2015; Cui et al., 2020). Different terrains distributed within YRB have important effects on the generation and reinforcement of mesoscale convective activities. The Eastward-Moving Southwest Vortex (EMSV) as typical Mesoscale Convective Vortex (MCV) originates from the southeastern slope of Tibetan Plateau, and have close relationship with the evolution of Mesoscale Convective Systems (MCSs). These two different scales of weather systems are frequently coupled (i.e. multi-scale EMSV system) and evolved into multi-scale EMSV system during the eastward-moving of Southwest Vortex. The Second-Step Terrain Region (SSTR) (marked with red dashed rectangle in Fig.1), a typical type of topography located in the middle reaches of YRB, plays critical roles in generating and strengthening the EMSV and the associated MCSs. Subsequently the reinforced EMSV and MCSs take dominant responsibilities for the frequent occurrence of severe rainstorms in the middle and lower reaches of YRB (Zhang et al., 2019). Therefore, further investigation of the topographical effect exerted by the SSTR is demanded for full understanding of the reinforcement mechanism of the multi-scale EMSV system, as well as the triggering mechanism of the local heavy precipitation.

It is frequently observed that the MCSs and the MCVs are mutually coupled in many local heavy precipitation events (Davis, et al., 2009). Previous study have confirmed that the genesis of MCV can be induced by the adiabatic cooling released by an MCS in the middle level of troposphere, whereas the advantageous ambient conditions provided by MCV is contrarily favorable for the prolongation of the

lifespan of MCSs (Houze, 2004). The MCV (Southwest Vortex is a typical type of MCV) and MCSs incorporated in the multi-scale EMSV system respectively regulate different scales of ambient circulation fields, and they have different responses to the topographical force of SSTR when the multi-scale EMSV system passed over SSTR, which subsequently brings more complexity to the interaction mechanism between MCVs and MCSs. Therefore, it is essential to investigate how the topographical effect affects the evolution of the Southwest Vortex and MCSs respectively based on the effective decomposition of the compound circulation incorporated into the multi-scale EMSV system into different scales of circulation that represent Southwest Vortex and MCSs, so that more accurate understanding of the topographical effect on the local heavy precipitation can be achieved.

Potential Vortex (PV) is a compound physical variable that can be applied to describe both dynamic and thermal properties of the atmospheric motion, which was first proposed by Rossby (1940). The PV theory is widely adopted in the analysis and diagnosis of the synoptic system due to its conservative property and inversion property. However, PV anomalies will be generated with non-adiabatic and frictional condition, then focus on revealing how the PV anomalies are generated can help advance the understanding of the evolution mechanism of some particular types of synoptic systems. Previous study reveals that the non-adiabatic heating and the frictional effect of the underlying surface are the direct causes for the genesis of the PV anomalies (Haynes, et al., 1987; Raymond, et al., 1992). And the non-adiabatic heating causes PV anomalies mainly by the following physical processes, including

78 the latent heat release associated with the convection, the evaporation on the ground
79 surface and the moisture condensation within the cloud. With exception of the above
80 factors, the topographical effect is another key factor for the genesis of the PV
81 anomalies. The PV anomalies can be generated by the breaking of the wave train in
82 the leeward of mountain, or by the split of the incident flow over the terrain,
83 subsequently the Von Karman vortex streets appear under the co-effect between the
84 PV anomalies in the air and the potential temperature anomalies on the ground surface,
85 and the persistence of the vortex streets provides favorable condition for the
86 occurrence of the subsequent severe convective weather (Schar,et al.,1997). Further
87 research discovered that the dynamical structure of PV anomalies band is closely
88 related with the topographical feature and the dynamic processes dominated by the
89 topographical effect (Schar,et al.,2003), which reconfirms the importance of the
90 topography in affecting the generation and the structure of PV anomalies. Therefore,
91 analyzing the topographical effect from the perspective of PV theory is a
92 recommendable approach to gain more in-depth understanding of the topographical
93 effect on multi-scale EMSV system.

94 The technique of Piecewise Potential Vortex Inversion (PPVI) is established
95 based on the inversion property of PV, which provides an effective approach to
96 decompose the compound circulation into different types of circulation. The PPVI
97 technique was first proposed by Eliassen and Klenschmidt(1957), and this innovative
98 discovery demonstrated excellent prospect in the diagnosis and the prediction of the
99 synoptic scale and the mesoscale of atmospheric motion at that time. Hoskins (1985)

presented detailed elaboration of the physical meaning of PPVI targeting for the practical application, building a solid foundation for the widespread application of PPVI. Different scales of circulation incorporated in some particular multi-scale synoptic systems, such as typhoon systems, Meiyu front systems, mesoscale vortex systems, are feasible to be abstracted from the compound circulation with PPVI. The further analysis of the decomposed circulations can help advance the understanding of the evolution mechanism of these high impact weather systems(Wang, et al., 2005; Zhang, et al., 2006; Zhao, et al., 2006; Ge, et al., 2011). Besides, to quantitatively diagnose the contribution of different types of circulation to the evolution of the coupling synoptic system based on the PPVI technique is another significant application of PPVI (Chen, et al., 2003; Fu, et al., 2019).

The complexity of the interaction mechanism between multi-scale EMSV systems and the topographical effect of SSTR results in the uncertainty of the topographical effect on the evolution of multi-scale EMSV systems. Therefore, advancing the understanding of the topographical effect of SSTR on the reinforcement of multi-scale EMSV system is in great demand as the enhanced multi-scale EMSV system often leads to catastrophic heavy rainfall events. To address this scientific issue, the following three steps are conducted in this paper: Step 1 is to select several representative multi-scale EMSV cases with similar origin locations, cyclonic circulation scale, and moving direction, and then conduct synthetic simulation based on the synthesis of these selected cases; Step 2 is to decompose the compound circulation of the multi-scale EMSV system simulated by the WRF model

into different scales of circulation, and investigate the evolution characteristics of these different scales of circulation under the topographical effect of SSTR; Step 3 is to investigate the linkage between these different scales of circulation and the distribution of PV anomalies induced by the topographical effect of SSTR; In Step 4, through qualitative sensitivity experiments and quantitative diagnosis, we will reveal the mechanism of how the PV anomalies are generated under the topographical effect of SSTR.

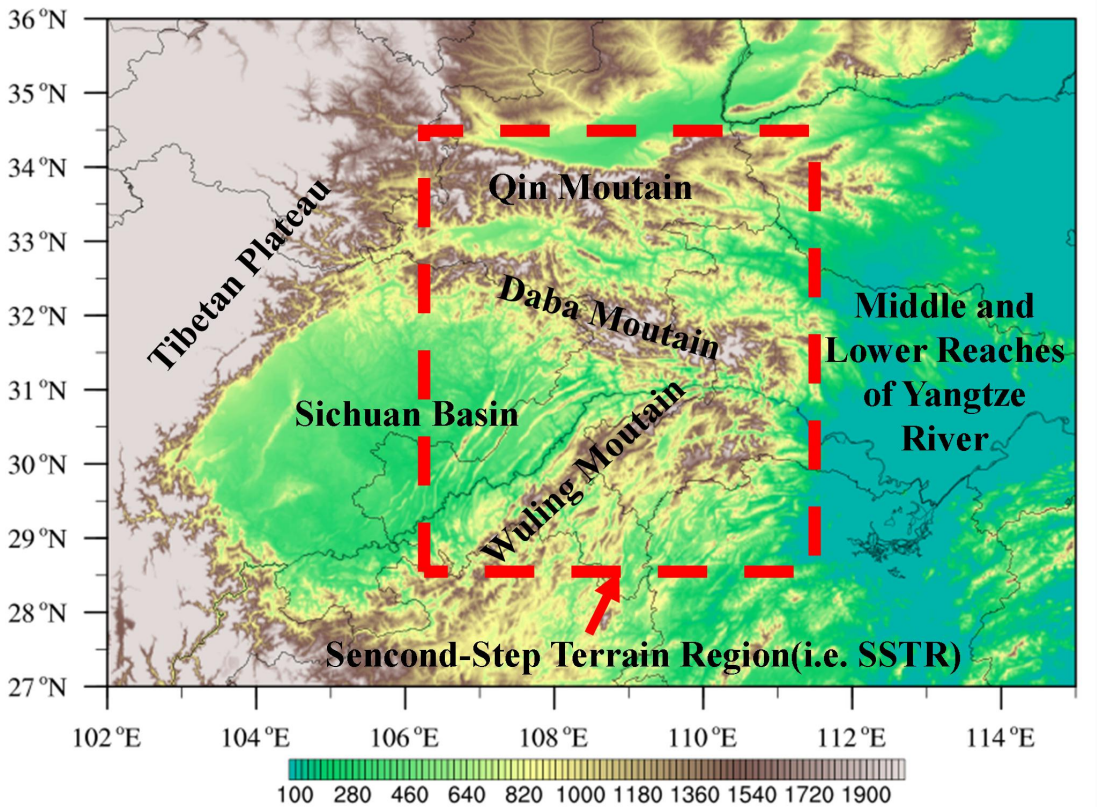

Fig. 1 The topographical map of the middle reaches of Yangtze River (The red dashed rectangle denotes the range of the Second-Step Terrain Region, shaded color denotes the altitude, unit: m)

2. Dataset and methodology

The primary data applied in this paper includes the Final Operational Global Analysis (FNL) data from National Centers For Environmental Prediction (NCEP)

with 6 h temporal and 1° × 1° spatial resolution, and the hourly fusion precipitation data merged from the rain gauge data and the CMORPH satellite data from the National Meteorological Information Center of China Meteorological Administration (NMIC/CMA). Since the accuracy of the gauge-based analysis relies on both density and configuration of the gauge network and the interpolation method. Thus satellite-based precipitation products generated by combining passive microwave (PMW) and infrared (IR) sensors are particularly useful over poorly gauged regions as they are capable in detecting spatial patterns and temporal variations of precipitation at a finer resolution. The improved datasets with hourly temporal resolution can better capture the variations of heavy weather events (Shen, et al. 2014).

Since the analysis of the topographical effect is based on the synthesis of the selected cases, the synthesis criterion needs to be first ascertained. Here, the synthesis approach mainly refers to taking the average of the selected cases at corresponding time respectively. As the start time, the end time and the lifespan for the selected cases are completely different from each other, the identification of the reference time (RT) for the synthesis of different cases becomes crucial. The RT in this paper is defined as the moment when the geopotential height center of EMSV on 700 hPa isobaric surface first enters the specified range (marked with blue rectangle in Fig.2). Then the synthesis results can be achieved by taking the average of the selected cases according to the RT and every 6 hours interval after RT. Furthermore, the initial field and the lateral boundary field to drive the WRF simulation of the synthesized multi-scale EMSV system can be provided by the above synthesis results. The detailed settings of

156 the physical parameters in the WRF model are shown in Table 1 (Mlawer, et al., 1997;
157 Dudhia, 1989; Hong, et al., 2006; Jimennez, et al., 2012; Milbrandt, 2005).

158 The PPVI theory shows superiority in the diagnosis of the thermal and dynamical
159 processes of the mesoscale vortex circulation due to its conservation and inversion
160 properties (Eliassen, et al., 1957). The key process to study the topographical effect of
161 SSTR in this paper highly depends on the decomposition of the compound circulation
162 incorporated in the multi-scale EMSV system, and the decomposition of the
163 compound circulation incorporated in the multi-scale EMSV system into different
164 scales of circulation is fundamentally based on the PPVI technique, so it is essential to
165 present detailed elaboration of the principle of the PPVI theory in this paper.

166 Ertel's PV is a conservative variable on the premise of the
167 frictionless and adiabatic heating condition (Rossby, 1940; Ertel, 1942), which is:

168 $$q = \frac{1}{\rho}\varsigma_a \cdot \nabla\theta \tag{1.1}$$

169 where q is Ertel's PV, ρ is the air density, ς_a is the absolute vorticity, ∇ is the
170 three-dimensional gradient operator, and θ is the potential temperature.

171 The quasi-geostrophic balance equation was first established by Charney (1955)
172 to describe the quasi-geostrophic motion for free atmosphere, which is:

173 $$\nabla^2\phi = \nabla \cdot f\nabla\psi + 2\left[\frac{\partial^2\psi}{\partial x^2}\frac{\partial^2\psi}{\partial y^2} - \left(\frac{\partial^2\psi}{\partial x\partial y}\right)^2\right] \tag{1.2}$$

174 where ϕ is the potential function, ψ is the stream function, and f is geostrophic

parameter.

If the horizontal wind defined in the Ertel's PV is replaced by the non-divergent wind and non-rotation wind, Eq 1.1 can be substituted with stream function ψ and potential function ϕ, which is:

$$q = \left[(f + \nabla^2 \psi) \frac{\partial^2 \phi}{\partial z^2} - \frac{\partial^2 \psi}{\partial z \partial x} \frac{\partial^2 \phi}{\partial z \partial x} - \frac{\partial^2 \psi}{\partial z \partial y} \frac{\partial^2 \phi}{\partial z \partial y} \right] \tag{1.3}$$

where ψ, ϕ, and q are compound variables here, which can be regarded as the constitution of the balanced component and the perturbed component, which are:

$$\psi' = \psi - \overline{\psi}, \quad \phi' = \phi - \overline{\phi}, \quad q' = q - \overline{q} \tag{1.4}$$

where $\overline{\psi}$ and $\overline{\phi}$ denote the balanced component of the variables, which represent the temporal average, while ψ' and ϕ' denote the perturbed component of the variables, which represent the surplus between the compound component and the balanced component.

For linearizing Eq. 1.2 and Eq. 1.3, these two equations are substituted with Eq. 1.4, and the final forms of Eq. 1.2 and Eq. 1.3 with simplified operations are presented as following:

$$\nabla_h^2 \phi' = f \nabla_h^2 \psi' + \beta \frac{\partial \psi'}{\partial y} + 2\left(\frac{\partial^2 \overline{\psi}}{\partial x^2} \frac{\partial^2 \psi'}{\partial y^2} - 2 \frac{\partial^2 \overline{\psi}}{\partial x \partial y} \frac{\partial^2 \psi'}{\partial x \partial y} + \frac{\partial^2 \overline{\psi}}{\partial y^2} \frac{\partial^2 \psi'}{\partial x^2} \right)$$

$$+ 2\left(\frac{\partial^2 \psi'}{\partial x^2} \frac{\partial^2 \psi'}{\partial y^2} - \left(\frac{\partial^2 \psi'}{\partial x \partial y} \right) \right) \tag{1.5}$$

$$q' = \left(f + \nabla_h^2 \overline{\psi}\right)\frac{\partial^2 \phi'}{\partial z^2} + \nabla_h^2 \psi' \frac{\partial^2 \overline{\phi}}{\partial z^2} - \frac{\partial^2 \overline{\psi}}{\partial x \partial z}\frac{\partial^2 \phi'}{\partial x \partial z} - \frac{\partial^2 \overline{\psi}}{\partial y \partial z}\frac{\partial^2 \phi'}{\partial y \partial z} - \frac{\partial^2 \psi'}{\partial x \partial z}\frac{\partial^2 \overline{\phi}}{\partial x \partial z} - \frac{\partial^2 \psi'}{\partial y \partial z}\frac{\partial^2 \overline{\phi}}{\partial y \partial z}$$

$$+ \nabla_h^2 \psi' \frac{\partial^2 \phi'}{\partial z^2} - \frac{\partial^2 \psi'}{\partial x \partial z}\frac{\partial^2 \phi'}{\partial x \partial z} - \frac{\partial^2 \psi'}{\partial y \partial z}\frac{\partial^2 \phi'}{\partial y \partial z} \quad (1.6)$$

The variables of q', f, $\overline{\psi}$, $\overline{\phi}$ in the above equations can be calculated out based on the WRF simulation results, while the variables of ψ' and ϕ' in Eq. 1.5 and Eq. 1.6 are the only two remaining variables that are waiting for solution. Since Eq. 1.5 and Eq. 1.6 jointly build up closed equations regarding ψ' and ϕ', thus the variables of ψ' and ϕ' can be surely solved. And the perturbed horizontal wind U' and V' can be solved by the combination of ψ' and ϕ', while the balanced horizontal wind $\overline{U}$ and $\overline{V}$ can be solved by the combination of $\overline{\psi}$ and $\overline{\phi}$.

Table 1. The settings of the physical parameters in WRF simulation

Horizontal Resolution	Grid Number	Microphysics Scheme	Longwave Radiation Scheme	Shortwave Radiation Scheme	Surface Layer Scheme	Land Lurface Scheme	Boundary Layer Scheme	Cumulus Convective Scheme
9km	**630×400**	**Milbrandt-Yau 2-moment scheme**	**RRTM scheme**	**Dudhia Scheme**	**Monin-Obukhov scheme**	**Thermal diffusion scheme**	**MYNN 2.5 level TKE scheme**	**Betts-Miller-Janjic scheme**

3. Case study background

3.1 The observed background circulation of each selected case

In order to reveal the topographical effect of SSTR on multi-scale EMSV systems, three representative cases with similar origin location, similar cyclonic circulation scale, and similar moving direction are selected from those high impact events occurred during 2015-2016. In details, the event for Case 1 approximately started at

206 1800UTC on April 30th and ended at 0000UTC on May 2nd in 2015, the event for
207 Case 2 approximately started at 0000UTC on August 18th and ended at 0600UTC on
208 August 19th in 2015, and the event for Case 3 approximately started at 0000UTC on
209 June 30th and ended at 0600UTC on July 1st in 2016. Fig. 2 shows the evolution
210 characteristics of the background circulation of these selected cases. These selected
211 cases can be synthesized into a whole one due to their common features, which is
212 capable in reflecting the common evolution characteristics of this type of EMSV
213 systems under the topographical effect of SSTR. As the reinforcement of multi-scale
214 EMSV system and the increase in local precipitation intensity are mainly
215 concentrated during the period from RT to RT+6h, this period is the main concerned
216 stage in this paper naturally.

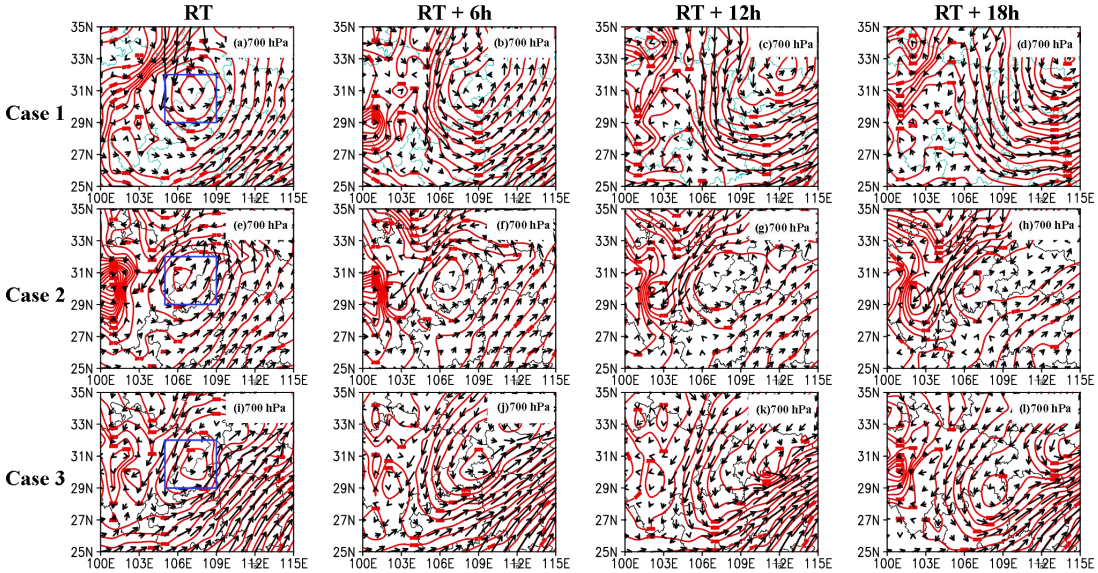

217 Fig. 2 The observation of wind (black vector, unit: m/s) and geopotential height (red contour, unit: gpm) derived from different cases of
218 multi-scale EMSV systems on the isobaric surface at 700 hPa (a-d: Case 1; e-h: Case 2; i-l: Case 3)

219 **4. Assessment of the synthesized simulation capacity**

220 It is demonstrated in Fig.3 that the synthesized simulation is capable in
221 reflecting the key features of the synthesized multi-scale EMSV system. To be
222 specific, the location of the multi-scale EMSV systems and the evolution of the
223 cyclonic circulation simulated by WRF agree well with the observation (Fig.3).
224 Besides, despite the disparities of the distribution of the precipitation between the
225 WRF simulation and the observation (located in the east and center of Hubei
226 Province), the local heavy precipitation distributed along the Wuling Mountain
227 (marked with gray rectangle in Fig.4) still demonstrates good agreement between the
228 WRF simulation and the observation. On account of the realistic representation of the
229 multi-scale EMSV systems and the local heavy precipitation, it is practicable to adopt
230 the WRF simulation to further investigate the topographical effect of SSTR.

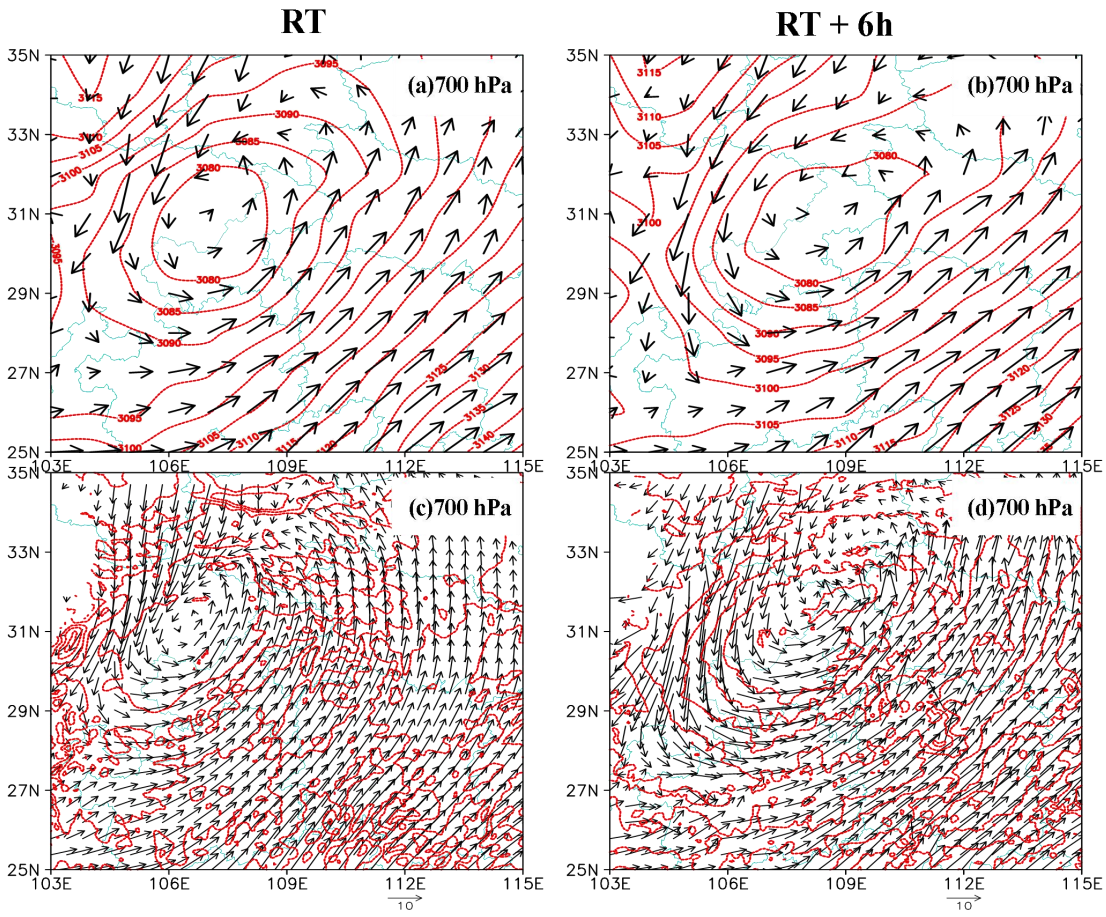

Fig. 3 The horizontal wind (black vector, unit: m/s) and the altitude (red contour, unit: m) of the observations (a, b) from the synthesis of the whole selected cases and the WRF simulation (c, d) at the moment of RT (left column) and RT+6h (right column) on the isobaric surface at 700 hPa

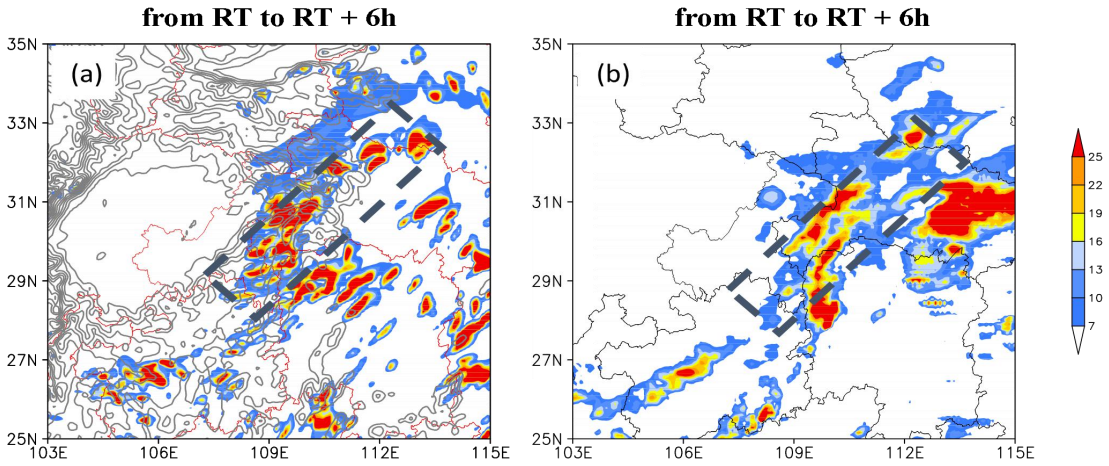

Fig.4 Comparison of the accumulated precipitation (colored, unit: mm) between the synthesized WRF simulation (a) and the synthesized CMORPH observation (b) during the period from RT to RT+6h (the gray contour in panel a represents the topographic isoline that exceeds over 800 m, the interval is 200 m)

5. Results

5.1 Decomposition of the compound circulation based on PPVI

From the perspective of PPVI theory, the compound circulation simulated by WRF primarily includes two different scales of circulation: the balanced circulation and the perturbed circulation. The balanced circulation is regulated by the balanced component of the stream function and the potential function, whereas the perturbed circulation highly depends on the perturbed component of the stream function and the potential function (more details presented in Section 2). It is clearly demonstrated in Fig. 5 that the balanced circulation can well capture the slow evolution of the meso-α scale cyclonic circulation (marked with red dashed vectors in the second column) in the multi-scale EMSV system, and the balanced circulation almost has no alteration when the local precipitation is intensified. In comparison, the perturbed circulation

249 can well characterize the quick replacement of the local scale cyclonic circulation
250 (marked with black dashed vectors in the third column) in the multi-scale EMSV
251 system, which has good agreement with the reinforcement of the local precipitation
252 intensity. Moreover, under the co-effect of the southwesterly wind dominated by the
253 Southwest Vortex and the topographical effect of SSTR, most of the local heavy
254 precipitation areas are approximately located along the Wuling Mountain. The meso-α
255 scale balanced circulation guarantees the abundant water vapor transportation, which
256 provides the essential moisture condition for the occurrence and the persistence of the
257 local heavy precipitation. However, the local scale perturbed circulation around the
258 heavy precipitation area takes direct responsibility for the occurrence of the local
259 heavy precipitation and provides the fundamental dynamical condition for the
260 intensification of the local precipitation. Considering the close relationship between
261 the perturbed circulation and the local heavy precipitation, identifying the factors that
262 determine and regulate the replacement of the perturbed circulation is the key issue
263 that needs to be addressed subsequently.

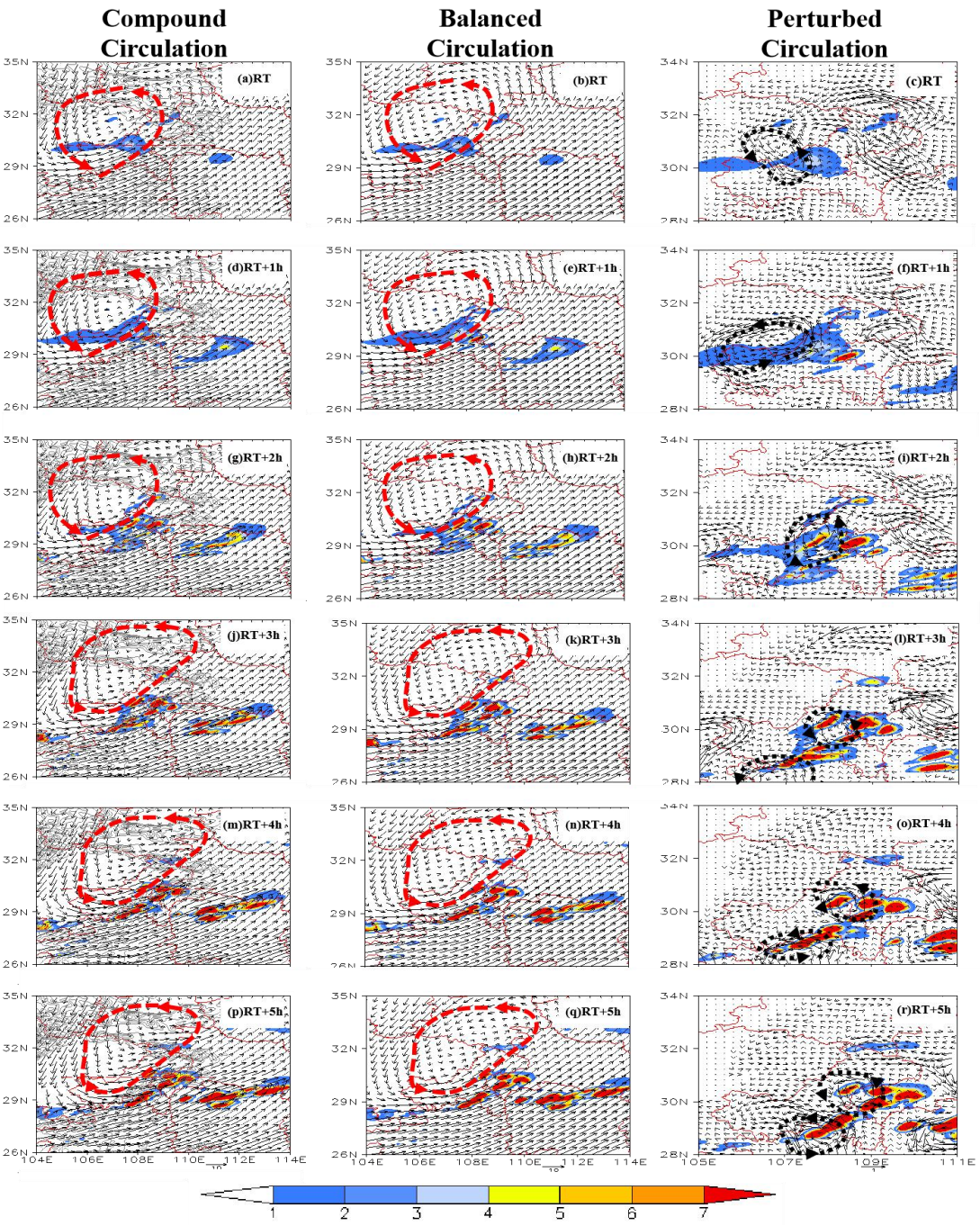

Fig. 5 Spatial distributions of hourly accumulated precipitation simulated by WRF (colored, unit: mm) and decomposition of the mixed circulation simulated by WRF (first column, vector , unit: m/s) into the balanced circulation (second column, vector arrow, unit: m/s) and the perturbed circulation (third column, vector arrow, unit:10^{-1} m/s) during the period from RT to RT+5h on 700 hPa isobaric surface

5.2 The good agreement between PV anomalies and perturbed circulation

The illustration of PPVI theory in Section 2 indicates that the perturbed circulation can be solved by the combination of the perturbed stream function and the

perturbed potential function, and both are closely associated with the perturbed PV, thus further investigation is needed to study the relationship between the perturbed circulation and the perturbed PV (defined as the PV anomalies here). It is shown in Fig. 6 that the PV anomalies and the perturbed circulation show good agreement with each other, especially around the local heavy precipitation area. The cyclonic perturbed circulation (marked with the black dashed vectors) happens to appear in the positive PV anomalies zone, which is observed on both 700 hPa isobaric surfaces (Fig. 6a - 6d) and 500 hPa isobaric surfaces (Fig. 6e - 6h). The stronger positive PV anomalies (denoted by colored) do cause stronger cyclonic perturbed circulation (marked with black dashed vectors) by the contrast between 700 hPa isobaric surface and 500 hPa isobaric surface. What should be paid more attention to is that the windward slope region is the most noticeable location where the positive PV anomalies are generated remarkably. Moreover, since the main concern and interest of the study is to reveal the topographical effect, it is essential to identify whether the topographical effect will lead to the formation of the positive PV anomalies. Further investigation on the mechanism of how the positive PV anomalies are generated within the topography region may help advance the understanding of topographical effect of SSTR.

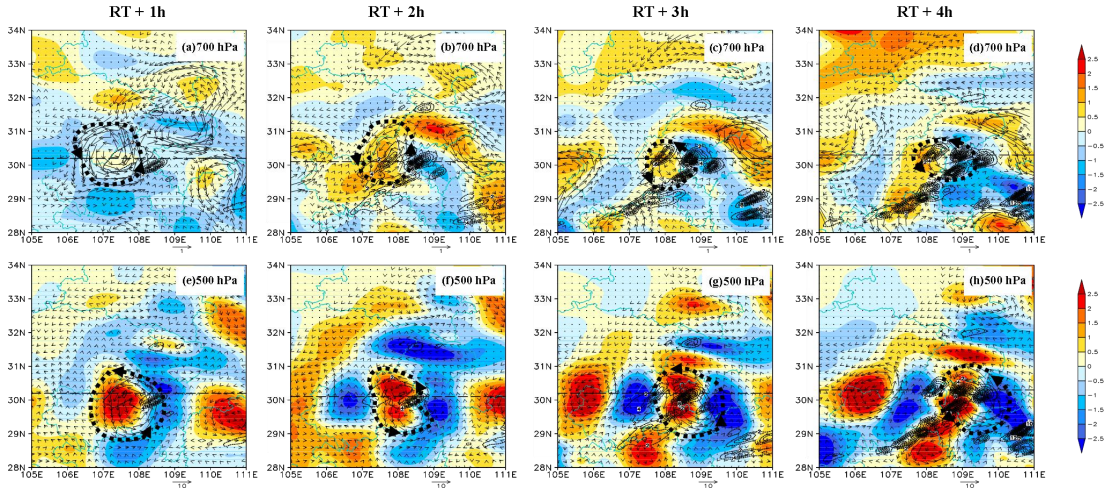

Fig. 6 Spatial distributions of the perturbed wind (black vectors, unit: m/s) and the PV anomalies (colored, unit: PVU, 1 PVU= $10^{-6}\cdot K\cdot s^{-1}\cdot Kg^{-1}$) on 700 hPa (a-d) and 500 hPa (e-h) isobaric surface (The black dashed line marks the location of the profile presented in the following section)

5.3 The vertical distribution of PV anomalies and its relevant variables

Previous study clearly pointed out that the PV anomalies are fundamentally determined by the variables including the potential temperature associated with the latent heat release, the cross-isentropic transport by the vertical wind and the absolute vorticity, which are incorporated in a diagnosed equation regarding the temporal variability of PV (Raymond, 1992). The vertical distributions of these variables demonstrate good agreement with each other in Fig. 7. From the figure, we can see that the increase of the latent heat release (contour in Fig.7a - 7d) is favorable for the genesis of positive PV anomalies (colored in Fig.7a - 7d), and the topographical effect of the windward slope does promote the increase of the latent heat release, which subsequently leads to stronger positive PV anomalies in the lower level of troposphere. In addition, it is confirmed that the vertical transportation of water vapor by the updraft (colored in Fig.7e - 7h) is directly responsible for the latent heat release

(contour in Fig.7e - 7h), and the topographical effect of the windward slope strengthens the updraft by the topographical lifting mechanism (denoted by gray dashed vectors in Fig. 7e - 7h), which accordingly results in the increase of the latent heat release. Moreover, positive feedback mechanism between the vertical wind (marked with contour line in Fig. 7i - 7l) and the relative vorticity (marked with shaded color in Fig. 7i - 7l) is observed as the changes in these two variables are well correlated with each other. The vertical stretch of the relative vorticity in the windward slope resulting from the blocking of the windward slope further promotes the strengthening of the updraft, causing more latent heat release and resulting in stronger positive PV anomalies indirectly.

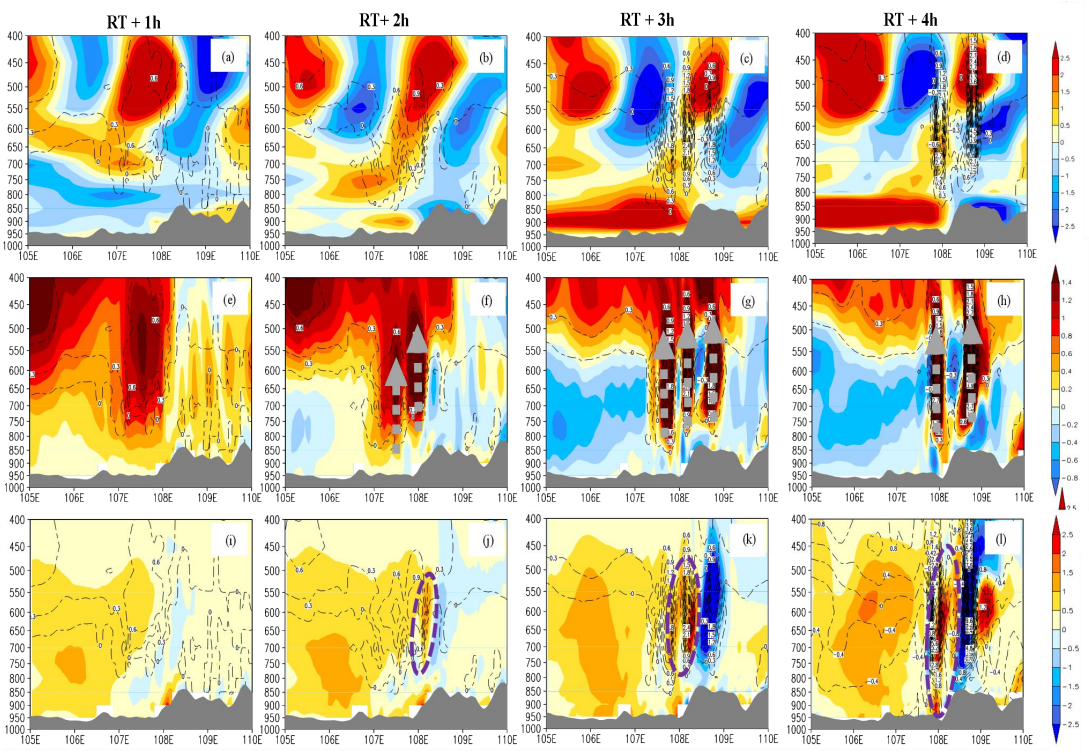

Fig. 7 Vertical profiles of the PV anomalies (colored in a - d, unit: PVU, 1 PVU=10-6·K·s-1·Kg-1), the latent heat release (black dashed contour in a - h, unit: kg/J), the vertical wind (colored in e - h, black dashed contour in i - l, unit: m/s), and the relative vorticity (colored in i - l, unit: 104 s-1)

5.4 Sensitivity experiments on different factors associated with the PV anomalies

5.4.1 Sensitivity experiment on the role of the latent heat release

A sensitivity experiment on the latent heat release (Fig. 8) is designed to further verify the critical role of the latent heat release in the genesis of the positive PV anomalies. The results show that the downward expansion of the positive PV anomalies is broken down with no latent heat release in the windward slope region (the black dashed oval in Fig. 8f - 8h). Moreover, the promotion of the positive PV anomalies by the latent heat release is nearly limited in the middle and low levels of troposphere (below 550 hPa isobaric surface). In other words, the positive PV anomalies in the high level of troposphere (above the isobaric surface of 550 hPa) seem to be less influenced by the removal of the latent heat release in the sensitivity experiment, which means the latent heat release is not the dominant factor for the generation of the positive PV anomalies in the high level of troposphere. In summary, the increase of the latent heat release induced by the topographical effect can promote the continuous genesis of the positive PV anomalies in the middle and low level of troposphere and the downward expansion of positive PV anomalies, which accordingly guarantees the persistence of the cyclonic perturbed circulation in these levels of troposphere.

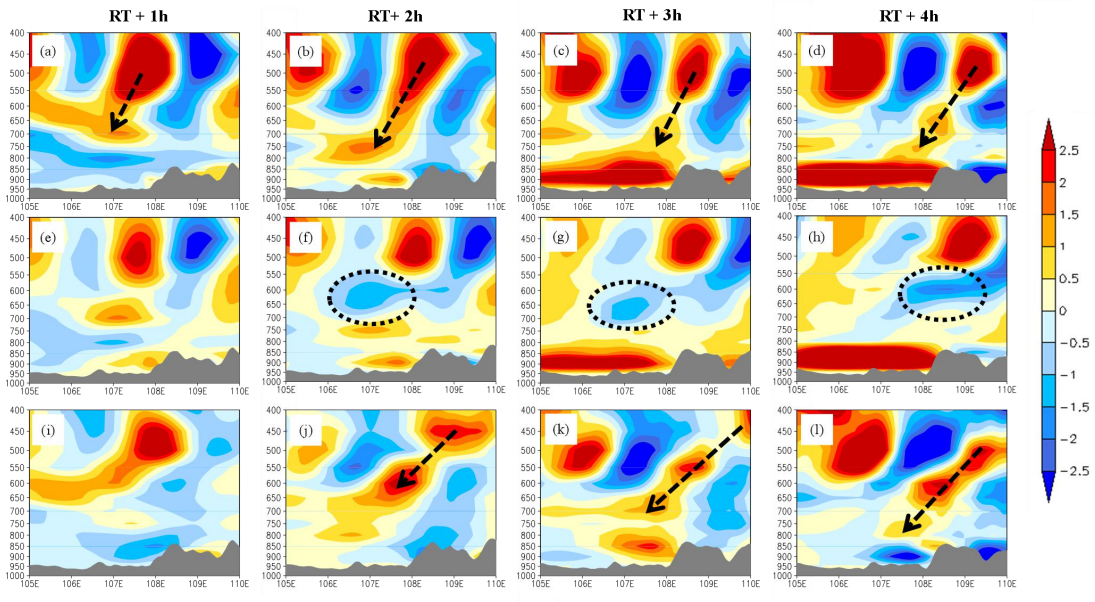

Fig. 8 Sensitivity experiment on the effect of the latent heat release on the genesis of PV anomalies in the vertical profile(a - d: control experiment; e - h: sensitivity experiment with no the latent heat release; i - l: the difference between the control experiment and the sensitivity experiment; colored: PV anomalies, unit: PVU, 1 PVU=10^{-6}·K·s^{-1}·Kg^{-1})

5.4.2 Sensitivity experiment on the topographical effect of the windward slope

As the significant topographical effect on the genesis of the positive PV anomalies is confirmed in previous section, the sensitivity experiment on the topographical elevation is designed to explore how the topographical effect associated with topographical elevation influences those key factors that are crucial for the genesis of the positive PV anomalies, including the velocity of the vertical wind, the latent heat release, and the relative vorticity. The difference between the control experiment and the sensitivity experiment indicates that the strength of the updraft (colored in the dashed oval in Fig. 9) in the windward slope region is remarkably weakened from the middle level to the low level of troposphere, and the latent heat release (black dashed line in the dashed oval in Fig. 9) is weakened accordingly with the removal of the topography in the sensitivity experiment. Besides, the blocking of

air mass in front of the windward slope region causes the reinforcement of the relative vorticity (colored in the dashed triangle in Fig. 10). Similarly, the relative vorticity is weakened likewise with the removal of the topography in the sensitivity experiment. Furthermore, the stretch of the relative vorticity resulting from the blocking of the windward slope does contribute to the strengthening of the updraft (black dashed line in the dashed oval in Fig. 10) from the middle level to the low level of troposphere in the control experiment, while the updraft is significantly weakened as the relative vorticity decreases in the sensitivity experiment.

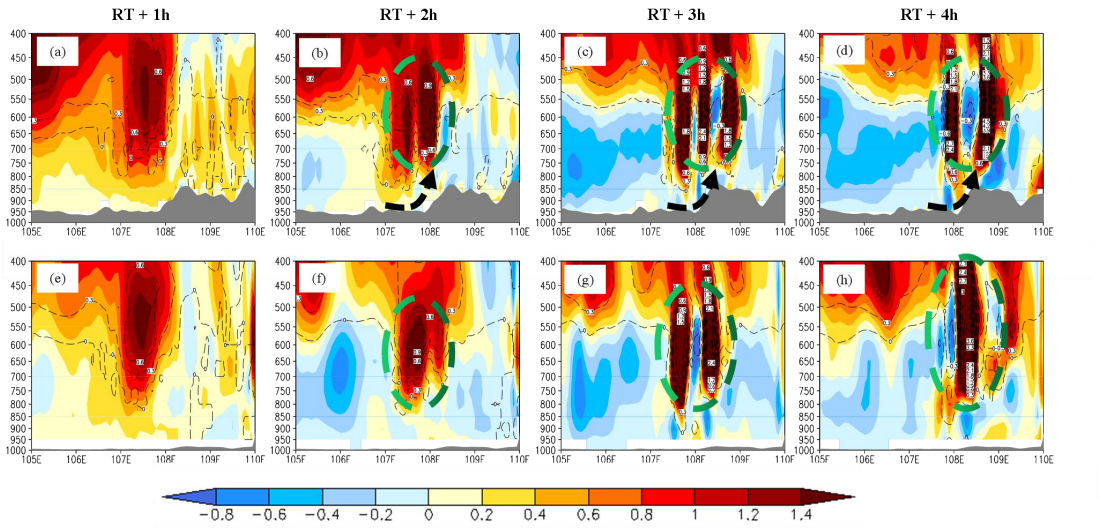

Fig. 9 Sensitivity experiment of the terrain elevation on the velocity of vertical wind (colored, unit: m/s) and the latent heat release (black dashed line, unit: kg/J) in the vertical profile (a - d: control experiment; e - h: sensitivity experiment in which the terrain elevation is reduced by ten times)

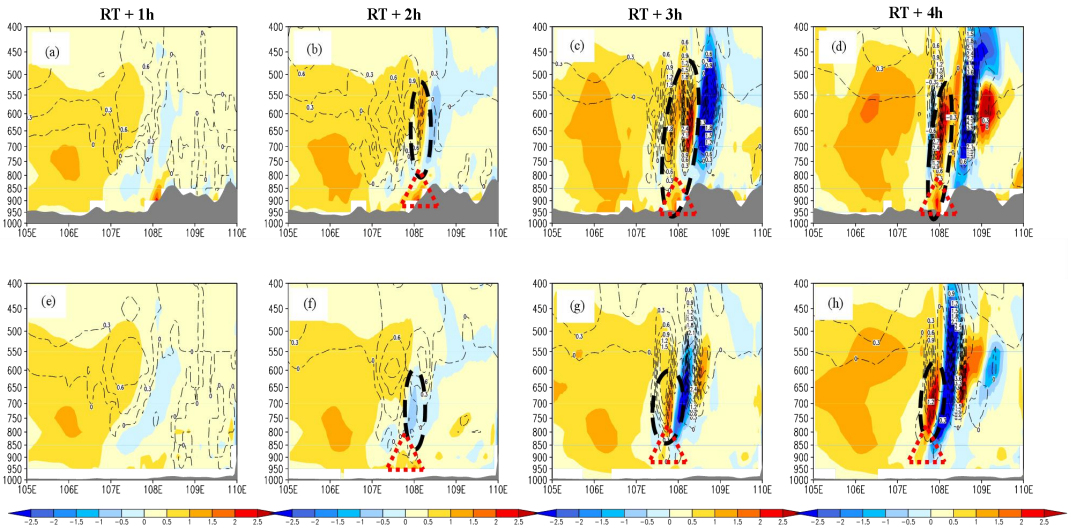

Fig. 10 Sensitivity experiment of the terrain elevation on the velocity of vertical wind (black dashed line, unit: m/s) and the relative vorticity (colored, unit: 10^4 s^{-1}) in the vertical profile (a - d: control experiment; e - h: sensitive experiment in which the terrain elevation is reduced by ten times)

5.4.3 Sensitivity experiment on the surface frictional dissipation

As the surface frictional dissipation is another significant factor for the generation of the PV anomalies, the sensitivity experiment on the surface friction is designed to verify the role of the surface friction in the genesis of the PV anomalies. It is demonstrated in Fig.11 that the genesis of the PV anomalies weakens with the friction velocity ust* (ust* is applied in the PBL scheme of WRF to describe the effect of surface friction on the atmosphere) increased by five times in the sensitivity experiment, which indicates that the effect of the surface frictional dissipation has negative feedback on the generation of PV anomalies. Moreover, we can see from the figure that the influence of the surface frictional dissipation is strictly limited below 850 hPa (black dashed oval in Fig.11), meanwhile the effect of the surface frictional dissipation is not the primary inducement to the generation of the positive PV anomalies in the middle and high levels of troposphere. In conclusion, the above

sensitive experiment suggests that when we investigate which factor has the major impact on the genesis of the positive PV anomalies above 850 hPa isobaric surface, the surface frictional dissipation effect on the genesis of PV anomalies can be neglected as the positive PV anomalies are less influenced by the frictional effect therein.

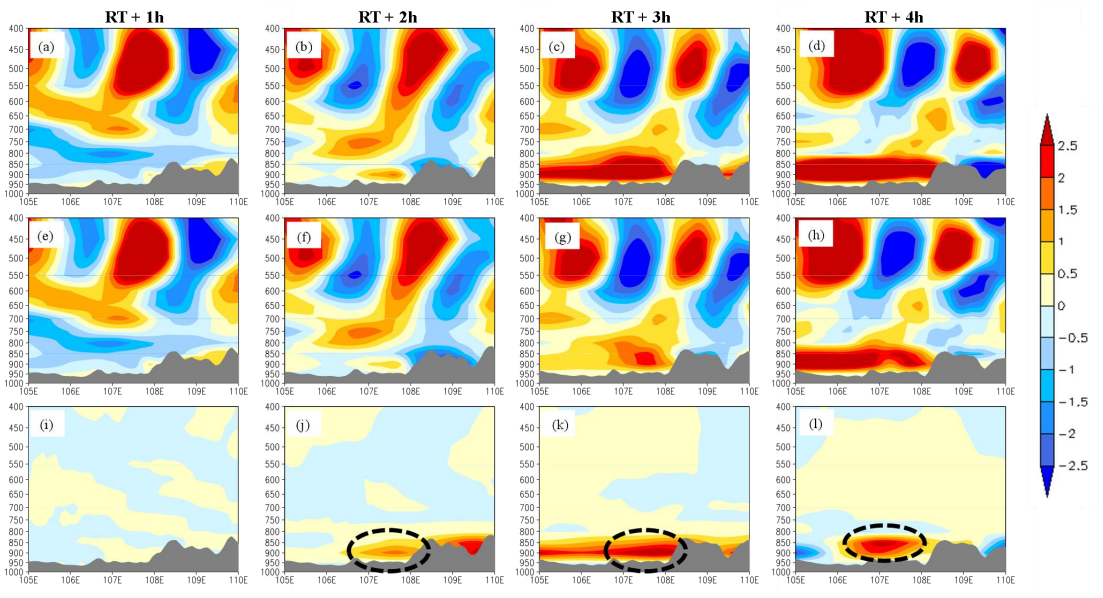

Fig. 11 Sensitivity experiment of the surface frictional dissipation effect on the genesis of the PV anomalies in the vertical profile (a - d: control experiment; e - h: sensitivity experiment in which the friction velocity increased by five times; i - l: difference between the control experiment and the sensitivity experiment; colored: PV anomalies, unit: PVU, 1 PVU = 10^{-6}·K·s^{-1}·Kg^{-1})

5.5 Quantitative diagnosis of the source of the PV anomalies

A series of sensitivity experiments are designed to discuss the roles of these above factors in the generation of PV anomalies. However, the results of these sensitivity experiments are mainly qualitative, only affirming the indispensable roles of these factors in the genesis of PV anomalies. Hence, more detailed quantitative diagnosis of the topographical effect is required to identify which factor plays the

391 dominant role in the generation of PV anomalies. The factors including the adiabatic
392 heating by the latent heat release, the vertical advection driven by the vertical wind,
393 the horizontal advection driven by the eddy flow and the surface frictional dissipation
394 effect (Raymond, et. al, 1990; Raymond, 1992; Peter et. al, 1999) are all taken into
395 consideration to systematically establish a diagnosed equation (shown as Eq. 2.3)
396 regarding the temporal variability of PV. Then the contributions of these factors to the
397 temporal variability of PV are precisely assessed based on this quantitative diagnosed
398 equation.

399 The diagnosed equation regarding the temporal variability of PV is presented as
400 the following:

401 $$\frac{dq}{dt} = \rho^{-1}\nabla \cdot (H\zeta_a + \nabla\theta \times F) \tag{2.1}$$

402
Where q is the potential vortex, F is the friction, ζ_a is the absolute vorticity, θ is the
403
potential temperature. H in Eq. 2.1 represents the adiabatic heating rate, which can be
404
furthered defined as:

405 $$H = w\left(\frac{\partial\theta_p}{\partial z}\right) \tag{2.2}$$

406
where w represents the velocity of vertical wind, then Eq. 2.1 is substituted with Eq.
407
2.2, and the final form with simplification is given below:

408 $$\frac{dq}{dt} = \rho^{-1}\zeta_z\left(\frac{\partial w}{\partial z}\right)\frac{\partial\theta_p}{\partial z} + \rho^{-1}w\left(\frac{\partial\zeta_a}{\partial z}\right)\frac{\partial\theta_p}{\partial z} + \rho^{-1}\nabla\cdot(\nabla\theta\times F) \tag{2.3}$$

409 ① ② ③

Where the three different terms ①, ②, ③are corresponding to the absolute vorticity term targeted for the characterization of the latent heat release driven by the horizontal eddy flow, the vertical velocity term targeted for the characterization of the latent heat release driven by the vertical wind, and the friction term targeted for the characterization of the frictional dissipation effect respectively.

As previous sensitivity experiment has confirmed that the effect of the surface frictional dissipation on the genesis of the PV anomalies can be neglected above 850 hPa isobaric surface, and the quantitative diagnosis is focused on revealing the genesis mechanism of the PV anomalies above 850 hPa isobaric surface, thus the quantitative diagnosis regarding the frictional dissipation term can be ignored here. More details of the quantitative diagnosis of the absolute vorticity term and the vertical velocity term are shown in Fig.12. In the early period (the period from RT+1h to RT+2h), the contributions of the absolute vorticity term and the vertical velocity term both keep in a low level. And in the later period (the period from RT+3h to RT+4h), the level of the contribution of the two terms almost have no alteration in the region that is distant from the topography region, while the level of the contribution of the two terms have a remarkable growth within the topography region, moreover, the contribution of the vertical velocity term is slightly higher than that of the absolute vorticity term. On the whole, the positive value of the sum of these two terms within the topography region guarantees the genesis of the positive PV anomalies within the topography region, which is consistent with the findings revealed in the topography sensitivity experiment. Further investigation reveals the linkage between the vertical

velocity term and the absolute vorticity term. To be specific, the blocking of the windward slope leads to the accumulation of the air at the foot of the mountain, which in turn forces the updraft associated with the vertical velocity term to intensify, resulting in the reinforcement of the ambient wind convergence based on the continuity of atmospheric motion, and the cyclonic eddy flow associated with the absolute vorticity term gradually arises and strengthens accompanied by the reinforcement of the ambient wind convergence accordingly.

Due to the critical role of the vertical wind in determining the temporal variability of PV, further quantitative diagnosis is performed to reveal the mechanism of how the topographical effect affect the variation of the vertical wind. It is reported in previous study (Yue, et al., 2013) that the topographical effect has two fundamental mechanisms to generate or reinforce the vertical wind, one is the topographical lifting effect, and the other is the boundary layer convergence effect. These two effects are both taken into account to establish a quantitatively diagnosed equation to investigate the linkage between the topography and the vertical wind. The diagnosed equations are presented below:

$$W = W_L + W_F \tag{3.1}$$

where W_L is the vertical wind driven by the topographical lifting effect, W_F is the vertical wind driven by the boundary layer convergence effect, and these two terms can be further defined as:

$$W_L = u\frac{\partial h}{\partial x} + v\frac{\partial h}{\partial y} \tag{3.2}$$

$$W_F = \frac{1}{f}\left[\frac{\partial}{\partial x}\left(C_d v\sqrt{u^2+v^2}\right) - \frac{\partial}{\partial y}\left(C_d u\sqrt{u^2+v^2}\right)\right] \quad (3.3)$$

Where h in Eq. 3.2 is the topography elevation, f in Eq. 3.3 is the geostrophic parameter, which is constant for the mesoscale and microscale atmospheric motion over the mid-latitude zone, and Cd in Eq. 3.3 represents the drag coefficient, which is constant as well. Then the quantitative diagnosis of these two different effects is performed based on Eq. 3.2 and Eq. 3.3 respectively, and the results are shown in Fig. 13. It is shown that the vertical wind driven by the topographical lifting effect and the boundary layer convergence effect both have remarkable growth within the topography region. However, the strengthening of the vertical wind driven by the topographical lifting effect is significantly higher than that driven by the boundary layer convergence effect. This suggests that the topographical lifting effect of the windward slope is the dominant mechanism to generate the positive PV anomalies that are responsible for the persistence of the cyclonic perturbed circulation, while the boundary layer convergence effect becomes the secondary one accordingly.

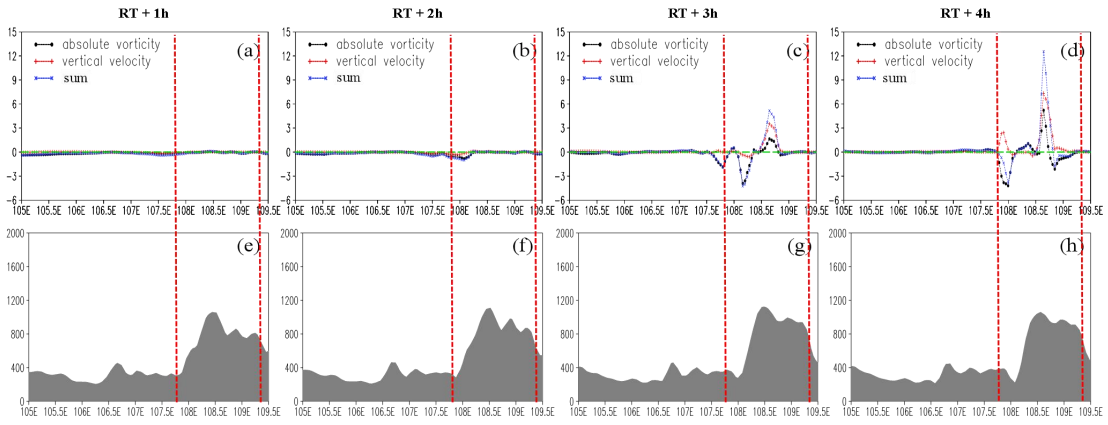

Fig. 12 Quantitative diagnosis of the absolute vorticity term (a-d, black line, unit:$10^{-5}\cdot K\cdot s^{-2}\cdot Kg^{-1}$), the vertical velocity term (a-d, red line, unit:$10^{-5}\cdot K\cdot s^{-2}\cdot Kg^{-1}$) and the sum of these two terms (a-d, blue line, unit:$10^{-5}\cdot K\cdot s^{-2}\cdot Kg^{-1}$) regulated by the topography (e - h, unit: m) to the genesis of the PV anomalies on 700 hPa isobaric surface (The red dashed line marks the range of topography region)

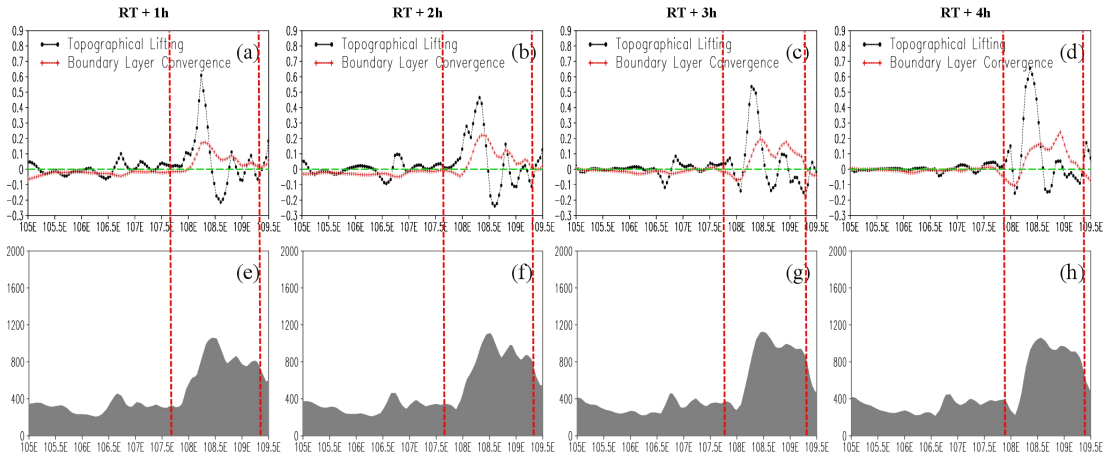

Fig. 13 Quantitative diagnosis of the vertical wind speed (on the surface ground) associated with the topographical lifting effect (black line in a - d, unit: m/s) and the boundary layer convergence effect(red line in a-d, unit: m/s) regulated by the topography (e - h, unit: m) (The red dashed line marks the range of the topography region)

6. Conclusion and Discussion

The long-term observation of geostationary satellite confirms that the mesoscale convection activities are highly active in the latitude zone of 30° N, where most of YRB is located. Different terrains distributed within the YRB play a significant role in the generation and the reinforcement of both eastward-moving MCSs and EMSV. The eastward-moving MCSs and the EMSV are mutually coupled and evolved into multi-scale EMSV systems during the eastward moving of the synoptic system. Among these complex terrain regions, the SSTR located in the eastern part of the Sichuan Basin is responsible for the significant strengthening of multi-scale EMSV systems when this type of synoptic system passes over. In this paper, we have focused on studying the mechanism of how the topographical effect of SSTR govern the evolution of the multi-scale EMSV system and its associated precipitation from the perspective of PV theory.

Three multi-scale EMSV system cases with similar origin locations, similar

cyclonic circulation scale, and same moving direction are selected from those high impact weather events occurred in 2015 and 2016. The WRF simulation targeted for the synthesis of these selected multi-scale EMSV system cases is capable in reflecting the common evolution characteristics of the multi-scale EMSV system and the common topographical effect of SSTR on the synoptic system. Based on the PPVI theory, the compound circulation simulated by WRF is decomposed into the balanced circulation and the perturbed circulation. The analysis of the two different types of circulations mentioned above provides a distinctive insight into the topographical effect of SSTR. The results indicate that the balanced circulation well capture the meso-α scale cyclonic circulation, which provides the essential moisture condition for the occurrence of the local heavy precipitation, while the perturbed circulation mainly demonstrated local scale cyclonic feature, which provides the direct dynamic condition for the occurrence of the local heavy precipitation. Moreover, the perturbed circulation has quicker response to the topographical force than the balanced circulation. The good agreement between the cyclonic feature of the perturbed circulation and the distribution of the local heavy precipitation confirms that the cyclonic perturbed circulation is conducive to the occurrence of the local heavy precipitation. Further analysis shows that the persistence of the cyclonic perturbed circulation is closely associated with the positive PV anomalies. Therefore, the mechanism of how the positive PV anomalies are generated under the topographical effect of SSTR becomes the key issue to be addressed here.

By performing a series of sensitivity experiments, the factors including the latent

heat release, the vertical wind and the relative vorticity are confirmed to have critical roles in the genesis of positive PV anomalies. Besides, the sensitivity experiment on the topographical elevation illustrates that the topographical effect has an indirect impact on the genesis of positive PV anomalies mainly by reinforcing the factors mentioned above. Also, it is found in the sensitivity experiment that the surface frictional dissipation effect on the genesis of the positive PV anomalies is strictly limited below 850 hPa isobaric surface. Then the quantitative diagnosis is performed to validate the findings revealed by the sensitivity experiments. It is reported in previous study that the source of the PV anomalies primarily includes two aspects: One is origin from the latent heat release driven by the vertical wind (denoted by the vertical velocity term), another one is origin from the latent heat release driven by the horizontal eddy flow (denoted by the absolute vorticity term). The diagnosis results show that the topographical force can reinforce both of these two aspects. However, the latent heat release driven by the vertical wind contributes more to the temporal variability of PV in the topography region than that driven by the horizontal eddy flow. Further diagnosis is performed to explore the linkage between the vertical wind and the topographical effect. The results show that both the topographical lifting effect and the boundary layer convergence effect do have impacts on the variation of the vertical wind, but the former one is the dominant mechanism whereas the latter one is the secondary mechanism for the strengthening of the updraft by the quantitative contrast of the two effects. Finally, to provide an intuitive understanding of the revealed mechanisms, all the above findings are briefly visualized with the schematic

diagram and the associated illustration shown in Fig. 14.

Several new findings regarding the topographical effect of SSTR on the multi-scale EMSV system are revealed in this paper, this research not only broadens the understanding of the interaction mechanism between the complex terrain and the PV anomalies, but also provides an innovative approach to reveal the topographical effect on the multi-scale EMSV system from the perspective of PV theory. The findings regarding the topographical effect in this paper highlight the topographical lifting mechanism of the windward slope. Compared to the previous research on the topographical lifting mechanism, the innovation of this paper lies in that it has revealed the indirect connection between the topographical lifting mechanism and the occurrence of the local heavy precipitation, from the perspective of PV theory, we have respectively revealed the mechanism of how the topographical effect causes the PV anomalies and how the PV anomalies govern the evolution of the multi-scale EMSV system, ultimately the indirect connection between the topographical lifting mechanism and the occurrence of the local heavy precipitation is effectively built based on the above analysis. Despite some innovative findings revealed in this paper, there are still some limitations existing in the present analysis. Firstly, the analysis based on the synthesized simulation of these selected cases only revealed some common features of the topographical effect on the multi-scale EMSV cases with long lifespan, yet the characteristics of those ones with short lifespan are remained to be studied. Thus future study on the topographical effect on the short lifespan EMSV is required. Secondly, the study in this paper is focused on revealing the topographical

553 effect on the genesis of the PV anomalies. Still, the results may vary in terms of
554 different categories of topographical force. To be specific, the study only reveals the
555 topographical effect of the windward slope on the multi-scale EMSV system, but the
556 topographical effect associated with other topographies in SSTR, such as leeward
557 slope, mountain valley, may be vastly different from the windward slope, so further
558 study is demanded to thoroughly understand the topographical effect of SSTR. Finally,
559 the study in this paper only investigates the mechanism of how the topographical
560 effect affects the evolution of the balanced circulation and the perturbed circulation
561 respectively. However, the mutual coupling of the balanced circulation and the
562 perturbed circulation determines the crucial role of the interaction between these two
563 different types of circulation in the evolution of multi-scale EMSV system, but the
564 study on the mechanism of how the topography affects the interaction mechanism is
565 not involved in this paper. Therefore, it is also required further investigation on how
566 the topographical effect affects the interaction mechanism between these two different
567 types of circulation. In brief, more in-depth research on the interaction mechanism
568 between different types of the decomposed circulation, and more overall investigation
569 of the topographical effect associated different multi-scale EMSV systems and
570 different topographies within SSTR are in demand in order to better understand the
571 topographical effect of SSTR in the future.

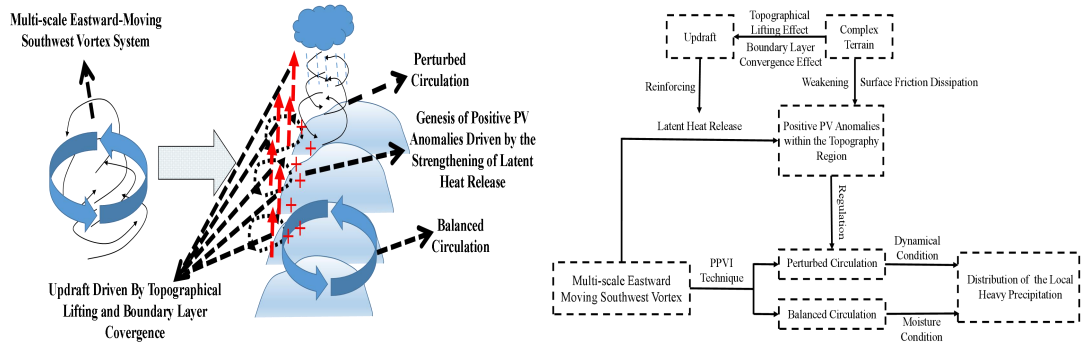

572 Figure 14 The schematic diagram (left) and the associated illustration (right) of how the topographical effect govern the evolution of the
573 multi-scale EMSV system and its associated precipitation from the PV theory

574 **Acknowledgments.** This work was supported jointly by the Integration Project of
575 Major Research Program of National Natural Science Foundation of China (Grant nos.
576 91937301), the National Natural Science Foundation of China (Grant nos. 41975058,
577 4210050695) and the National Key R&D Program of China (Grant no.
578 2018YFC1507200). The original FNL data are available from the RDA
579 (https://rda.ucar.edu) in dataset number ds083.2. The CMORPH hourly fusion
580 precipitation data were downloaded from the National Meteorological Information
581 Center (http://data.cma.cn).

References

A. Eliassen, E. Krishnamurti (1957). Dynamic meteorology. Berlin: Handbuch der Physik,48,112-129.

C. A. Davis and T. J. Galarneau JR (2009). The vertical structure of Mesoscale Convective Vortices. J. Atmos. Sci.,66:686-704.

C. G. Rossby (1940). Planetary flow patterns in the atmosphere. Q. J. R. Meteorol. Soc.,66,68-87.

C. Li, Y. Li, X. Jiang (2015). Statistical characteristics of the inter-monthly variation of the Sichuan Basin Vortex and the distribution of daily precipitation. Chinese Atmos. Sci., 39 (6): 1191−1203.

C. Schar and D. R. Durran (1997). Vortex formation and vortex shedding in continuously stratified flows past isolated topography. J. Atmos. Sci.,54:534-554.

C. Schar, M. Sprenger, D. Luthi, et al (2003).Structure and dynamics of an Alpine potential-vorticity banner. Q. J. R. Meteorol. Soc.,129:825-855.

C. Yue, J. Li, P. Chen, et al (2013). Study on improvement of moist Q vector interpretation technique. Chinese Plat. Meteor., 32(6):1617-1625.

D. J. Raymond and H. Jiang (1990). A theory for long-lived mesoscale convective systems. J. Atmos. Sci.,47(24):3067-3077.

D. J. Raymond (1992). Nonlinear balance and potential vorticity thinking at large Rossby number, Q. J. R. Meteor. Soc.,118:987-1015.

D. Zhang and C. Q. Kieu (2006). Potential vorticity diagnosis of a simulated hurricane. Part II:quasi-balanced contributions to forced secondary circulations. J. Atmos. Sci.,63:2898- 2914.

E. J. Mlawer, S J Taubman, P D Brown, et al (1997). Radiative transfer for inhomogeneous atmospheres: RRTM, a validated correlated-k model for the longwave. J. Geophys. Res. Atmos.,102(D14): 16663-16682.

G. T. Chen, C. C. Wang, S. C. Liu (2003). Potential vorticity diagnosis of a Mei-Yu front case. Mon. Wea. Rev.,131:2680-2696.

H. Ertel (1942). Ein neuer hydrodynamischer Erhaltungssatz. Die Naturwisssenschaften,36,543-544.

J Dudhia (1989). Numerical study of convection observed during the Winter Monsoon Experiment using a mesoscale two-dimensional model. J. Atmos. Sci.,46(20): 3077-3107.

J. A. Milbrandt, & M. K. Yau (2005). A multimoment bulk microphysics parameterization. Part Ⅱ: A proposed three moment closure and scheme description. J. Atmos. Sci., 62, 3065-3081.

J. G. Charney (1955). The gulf stream as an intertial boundary layer. PNAS, 41(10):731-740.

J. Ge,W. Zhong ,Hancheng Lu (2011). Diagnostic analysis of the quasi-balanced flow of a mesoscale vortex during the 12 June 2008 Guangxi Rainstorm.Acta Meteorological Sinica,25:188-202.

J. Sun, F. Zhang (2012). Impacts of mountain-plains solenoid on diurnal variations of rainfalls along the Mei-Yu front over the East China Plains. Mon. Wea. Rev.,140:379-397.

L. Zhang, J. Min, X. Zhuang, et al (2019). General Features of Extreme Rainfall Events Produced by MCSs over

East China during 2016-2017. Mon. Wea. Rev., 147: 2693-2714.

P. A. Jimenez, J Dudhia, J F Gonzalez, et al (2012). A revised scheme for the WRF surface layer formulation. Mon. Wea. Rev.,140:898-918.

P. H. Haynes and M. E. Mcintyre (1987). On the evolution of vorticity nd potential vorticity in the presence of diabatic heating and frictional or other forces. J. Atmos. Sci.,44:828-841.

Q. Wang and Z. Tan (2009). Idealized numerical simulation study of the potential vorticity banners over a mesoscale mountain: dry adiabatic process.Adv. Atmos. Sci.,26:906-922.

R. A. Houze Jr (2004). Mesoscale convective systems. Rev. Geophys., 42, doi:10.1029/2004RG000150.

R. Yang, Y. Zhang, J. Sun, et al (2019). The characteristics and classification of eastward-propagating mesoscale convective systems generated over the second-step terrain in the Yangtze River Valley. Atmos. Sci. Lett., 20:e874.

S. Fu, Z. Mai, J. Sun, et al (2019). Impacts of convective activity over the Tibetan Plateau on Plateau Vortex, Southwest Vortex, and downstream precipitation. J. Atmos. Sci., https://doi.org/10.1175/JAS-D-18-0331.1.

S. Y. Hong, Y Noh, J Dudhia (2006). A new vertical diffusion package with an explicit treatment of entrainment processes. Mon. Wea. Rev.,134(9):2318-2341.

T. M. Peter, J H Greg (1999). The role of potential vorticity generation in tropical cyclone rain bands. J. Atmos. Sci., 56:1224-1228.

W. Cui, X. Dong, B. Xi and M. Liu (2020). Cloud and precipitation properties of MCSs along the Meiyu frontal zone in central and southern China and their associated large-scale environments. J. Geophys. Res. Atmos. Atmos. 125(6), https://doi.org/10.1029/2019JD031601.

X. Wang and D. Zhang (2003). Potential vorticity diagnosis of a simulated hurricane. Part I:formation and quasi-balanced flow. J. Atmos. Sci.,60:1593-1607.

X. Yang, J. Fei, X. Huang, et al (2015). Characteristics of Mesoscale Convective Systems over China and its vicinity using geostationary satellite FY2. J. Climate, 28: 4890-4907.

Y. Shen, A. Xiong, Y. Wang, et al (2010). Performance of high-resolution satellite precipitation products over China. J. Geophy. Res.,vol.115, D02114, doi:10.1029/2009JD012097.

Y. Zhang, F. Zhang, C. A. Davis, et al (2018). Diurnal evolution and Structure of long-lived mesoscale convective vortices along the Mei-Yu front over East China Plains.J. Atmos. Sci.,75:1005-1025.

Y. Zhao, Z. Li, Z. Xiao, et al (2008). A PV inversion diagnostic study on a quasi-stationary Meiyu front with successive rainstorms. .Acta Meteorological Sinica.,65(3):353-371.

Y. Zheng, J. Chen, P. Zhu (2008). The distribution and diurnal variation of mesoscale convective systems occurred in China and its surrounding area in summer. Chinese Sci. Bull., 53(4):471-481.